

Accurate Checkerboard Corner Detection under Defocus

Zezhun Shi
Independent Researcher

Abstract

Camera calibration is a critical process in 3D vision, impacting applications in autonomous driving, robotics, architecture, and so on. This paper focuses on enhancing feature extraction for checkerboard corner detection, a key step in calibration. We analyze existing methods, highlighting their limitations and propose a novel sub-pixel refinement approach based on symmetry, which significantly improves accuracy for visible light cameras. Unlike prior symmetry based method that assume a continuous physical pattern, our approach accounts for abrupt changes in visible light camera images and defocus effects. We introduce a simplified objective function that reduces computation time and mitigates overfitting risks. Furthermore, we derive an explicit expression for the pixel value of a blurred edge, providing insights into the relationship between pixel value and center intensity. Our method demonstrates superior performance, achieving substantial accuracy improvements over existing techniques, particularly in the context of visible light camera calibration. Our code is available from [https://github.com/spdfghi/Accurate-Checkerboard-Corner-Detection-under-Defocus.git](https://github.com/spdfghi/Accurate-Checkerboard-Corner-Detection-under-Defocus).

1. Introduction

Camera calibration is fundamental to 3D vision, with broad applications in autonomous driving, robotics, architecture, medicine, etc. Camera calibration primarily serves two purposes: first, to establish a mapping between three-dimensional homogeneous coordinates (rays originating from the camera) and pixel points, known as intrinsic calibration; and second, to calibrate the positional relationship between the camera and other cameras [16, 34] or types of sensors, such as LiDAR [24], known as extrinsic calibration. Camera calibration methods are mainly divided into those based on target based calibration and online self-calibration methods [19], depending on the input. In certain scenarios, such as aerial robots, extrinsics can undergo significant changes even with moderate shocks or during extended operations in environments with vibrations, mak-

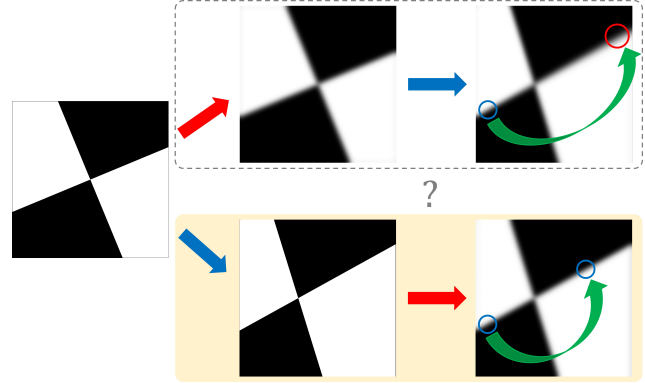


Figure 1. **Two ways of blur nature.** The leftmost section shows the ideal pattern for camera calibration, while the right section illustrates two ways a camera can capture a blurred image. In right part, the blue arrows indicate perspective effects, and the red arrows represent blurring. The top dashed box represents an infrared camera image where the first red arrow represents the smooth physical input due to thermal nature, and the blue arrow represents perspective effects when defocus is considered not important. While the bottom box shows an image captured by a visible light camera, where defocus is the dominant factor. The circles correspond to two regions in object space that are symmetric. The former is determined by the homography matrix, and for constant defocus, the latter remains symmetric.

ing self-calibration important. However, since intrinsic parameters remain relatively stable even in challenging conditions [34] and target based calibration accuracy advantage over self-calibration, they dominate in most scenarios and are a necessary preliminary step for multi-sensor extrinsic calibration.

In intrinsic calibration, the projection camera model with non-linear distortion terms commonly used today was proposed by Brown [6, 8], while Zhang established an effective method for calibration based on 2D plane point mapping [33], which is widely applied. Additionally, there are calibration methods based on line distortion correction [5] and general calibration methods [18, 25] that fully consider point and line mapping. Feature extraction is the first step of calibration, which ultimately determines the accuracy and is the focus of this paper. The two main types of

calibration targets are checkerboards and circles; checkerboards have the advantage of higher robustness to distortion, while circles offer higher accuracy [4, 14, 15]. The main issue with the circles pattern is that the shape of the circle under distortion can hardly be calculated. Recently, Song et al. [28] proposed an impressive analytical method to compute the centroid of a distorted circle and outperforms checkerboard-based calibration. But this method still has limitations, as extracting centroid in the image requires a larger pattern area than traditional circle fitting method, thus restricting the position of the circle’s center from the image edge, where distortion is most significant.

To improve the detection accuracy of checkerboard corner points, a series of methods have been studied. Currently, two mainstream approaches are notable. The first is assuming vector from a corner to its adjacent area pixel is orthogonal to pixel’s gradient direction, such as implemented in OpenCV [10], which achieve good sub-pixel accuracy; however, its performance is subpar under some conditions, as tested by Schöps et al. [27] and Song et al. [28] with infrared cameras. Datta et al. discovered that the assumption of OpenCV does not hold in non fronto-parallel input images [4]. Therefore they iteratively estimate the homography matrix, and then extract point after a transform to canonical fronto-parallel image, which result in a significantly improvement. The second approach involves quadratic surface fitting [20], commonly used in MATLAB. Fitting methods not only apply to regular checkerboards but have also been extended to curved surface[31]. Ha et al. [12] expanded the fitting method to patterns with three intersecting lines, and got better reprojection error than checkerboard which has two intersection lines. Schöps et al. [27] further developed Ha’s pattern by using a star-shaped calibration board with eight intersecting lines, they proposed a novel feature extraction algorithm for the pattern [26, 27], this method takes cost by pixel differences in projections of two world points that are symmetric about pattern center. With more gradient information, they got significant improvement in accuracy. They tested their method on the expanded checkerboard pattern using both RGB and infrared cameras, achieving reprojection errors that was reduced to 1/2 and 1/4, respectively, compared to the OpenCV method, which is impressive.

However, we are curious why their method shows such a significant difference between the RGB and infrared cameras, and is it possible that their method is not the most effective for the RGB cameras. We carefully considered their assumptions. First, their optimization objective function implicitly assumes that the image is captured by a pin-hole camera of a continuous physical pattern, and that there should not be significant distortion. Then, they assume that the image vary smoothly among neighbor pixels. Regarding the former, we believe that the assumption of a continuous

physical pattern does not always hold. For the infrared cameras, since infrared radiation is based on the spontaneous emission from the thermal motion of molecules, and it is almost impossible for the surface temperature of an object to change abruptly, the assumption of a continuous spatial pattern is reasonable. However, for the RGB cameras, which captures light reflected by objects and is related to the object’s color, abrupt changes can occur within the range of a single pixel[29]. For blurry images, defocus becomes the dominant factor. Thus, we proposed a novel objection function by consider this kind of blur, experiment of visible light camera shows agree with our assumption. Moreover, our objective function is simpler with fewer parameters, which means reduced computation time and a lower risk of overfitting. We also do a math on their smooth assumption by study a blur line model, which is the convolution of 2D step function with a Gaussian kernel. The closest model to the one we used is Ref. [1], where they addressed constructing feature detector. We provided explicit expression for pixel value the first time and used it to study the variation of differences against intensity of pixel center.

As a summary, there are two main contributions of this paper:

- We propose a novel sub-pixel refinement method for checkerboard corner detection based on symmetry and provide a detailed analysis of its physical assumptions. This method shows significant accuracy improvements in visible light camera compared with existing symmetry based method and mitigates overfitting risks.
- For the first time, we derive an explicit expression for the pixel value (as a region integral) of an blur edge based on the convolution model of a 2D step function with a Gaussian kernel. Using this analytical result, we analyze the difference between the pixel value and the intensity at the pixel center.

2. Related Works

Camera Calibration under defocus Duda et al. [7] proposed a method based on a localized Radon transform approximated by box filters, compared to the OpenCV method, it is more robust to noise and blur, achieving significant accuracy improvements in outdoor environments. Ha et al. [11] introduced an active targets approach for calibration under defocus, they separated the checkerboard into overlapping horizontal and vertical stripes, and then applied a novel deconvolution method to these stripes. Further, they do a refraction correction of the glass screen. This method was evaluated on real data, and shows accurate camera calibration result under severe defocus.

Active target has also been applied in varies patterns, some researchers used phase information which they considered more robust in defocusing scenes than checkerboard [17, 21], and phase-shift method for camera cali-

bration has been developed in recent years. These methods mainly contains sets up sinusoidal stripes [32] or circular patterns [3] sequentially displayed on an LCD monitor and detect sub-pixel feature points from phase map, which is calculated by phase-shifting algorithm. And with neural network for feature extraction, progress has been made in difficult tasks such as large field-of-view stereo calibration [21].

Line Detection under Defocus. The classic Canny algorithm obtains single-pixel edges through non-maximum suppression, and Devernay et al. further refines edges to sub-pixel accuracy using quadratic fitting near maxima[30]. While these well-known methods assume edge is maxima of smooth function, Ref. [29] first considers the physical scenario of a straight edge partially falling within a pixel. By analytically integrating the area segmented by the line within one pixel, it shows the discontinuity of discrete pixels will generate bias with traditional gradient computation. But they didn't provide an analytical result considering defocus. The calibration pattern used by Ha et al. [11] can actually be considered as lines under defocus, where they proposed an deconvolution method but also without using analytical formula. The analytical expression for line defocus was first introduced in Ref. [22] and later used in Ref. [35] for single-image defocus estimation. Bakery et al. [1] considered the pixel value rather than point value expression, which was not addressed in Ref. [22]. The line defocus model used in this paper is similar to Bakery et al., the key difference is that their paper focused on using numerical methods to construct a feature detector. They only provided an integral form while we provide explicit results.

3. Method

3.1. Camera model

We briefly review the pinhole camera and distortion model, which will be used in our experiment part. For a point $[x_c, y_c, 1]^T$ in homogeneous representation of camera coordinate, the distorted point is represented as [8]

$$x_d = x_c(1 + k_1 r_c^2 + k_2 r_c^4 + k_3 r_c^6) + 2p_1 x_c y_c + p_2 (r_c^2 + 2x_c^2), \quad (1)$$

and

$$y_d = y_c(1 + k_1 r_c^2 + k_2 r_c^4 + k_3 r_c^6) + p_1 (r_c^2 + 2y_c^2) + 2p_2 x_c y_c, \quad (2)$$

where

$$r_c^2 = x_c^2 + y_c^2, \quad (3)$$

k_1, k_2, k_3 are radial distortion coefficients and p_1, p_2 are tangential distortion coefficients.

For modern, well-manufactured cameras, the shear deformation component can be ignored, and the camera model

takes the following form [13]

$$\mathbf{K} = \begin{bmatrix} f_x & 0 & c_x \\ 0 & f_y & c_y \\ 0 & 0 & 1 \end{bmatrix}, \quad (4)$$

the image coordinates can be obtained as

$$\begin{bmatrix} x_i \\ y_i \\ 1 \end{bmatrix} = \mathbf{K} \begin{bmatrix} x_d \\ y_d \\ 1 \end{bmatrix}. \quad (5)$$

3.2. Line defocus model

Before introducing our algorithm, we would like to discuss pixel continuity and the effect of image blur on interpolation. In the absence of blur, traditional subpixel techniques tend to produce significant deviations near image boundaries, which is the so called partial area effect[29]. A simple example involves two horizontally adjacent pixels, j and $j + 1$, with a vertical boundary dividing pixel j into two equal area, where the intensities of the two parts are W and B , respectively, while the intensity of all positions in pixel $j + 1$ is B . Using linear interpolation yields an intensity of $(W + 3B)/4$ at the location between the two pixels, which differs significantly from the true intensity B . Intuitively, Gaussian blur can reduce this discrepancy, and we will provide a quantitative discussion of this effect in this section.

Checkerboard feature points can be viewed as corner points where two lines intersect, we model the original image of line that captured by a noise-free pinhole camera as step function [1]

$$\mathcal{I}_o(\mathbf{p}|d) = \begin{cases} W, & d \geq 0 \\ B, & d < 0 \end{cases} \quad (6)$$

where W and B denote constant intensity of white and black region, and d represents the distance from point \mathbf{p} to the line passing through the feature center \mathbf{q} . Let θ denotes the angle from image x-axis to the line, one can compute d through a simple cross product

$$d(\mathbf{p}|\mathbf{q}, \theta) = (q_x - p_x) \sin \theta - (q_y - p_y) \cos \theta. \quad (7)$$

Note that the two half-planes divided by the line are not identical, so d is a signed quantity.

For optical camera, we need to consider the defocus factor and optical transfer function. Bakery et al. [1] modeled these effects as a Gaussian kernel function, which is a widely used [11, 22, 35] approach. 2-D Gaussian has the form

$$\mathcal{K}(x, y|\sigma) = \frac{1}{2\pi\sigma^2} e^{-\frac{x^2+y^2}{2\sigma^2}}. \quad (8)$$

The real blur image can be calculated as a convolution of noise-free pinhole image with the kernel. Due to the sym-

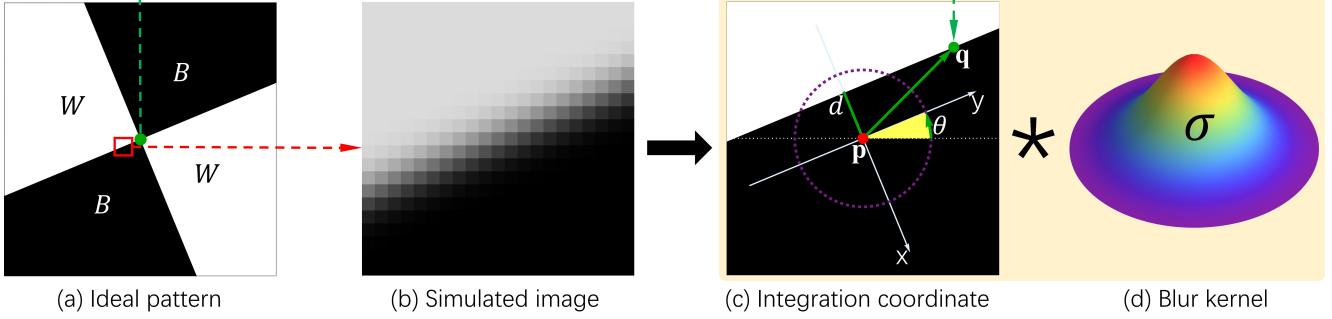


Figure 2. **Line defocus model.** (a) Ideal checkerboard pattern. (b) Simulation of the area near pattern center, generated using Eq. (13) with $W = 250$, $B = 50$, $\theta = \pi/8$, $\sigma = 1.5$ and $\mathbf{q} = (0, 0)$. (c) Coordinate system and parameters computed in Eq. (9). (d) 2-D Gaussian convolution kernel.

metry of Gaussian function, we align the y-axis with direction of the line (Fig. 2(b)-(d)), which simplifies the convolution to a straightforward integration

$$\begin{aligned}
& \mathcal{I}_b(\mathbf{p}|d, \sigma) \\
&= \mathcal{I}_o(\mathbf{p}|d) * \mathcal{K}(x, y|\sigma) \\
&= \frac{1}{\sqrt{2\pi\sigma^2}} \left[W \int_{-\infty}^d e^{-\frac{x^2}{2\sigma^2}} dx + B \int_d^{\infty} e^{-\frac{x^2}{2\sigma^2}} dx \right], \quad (9) \\
&= \frac{W - B}{2} \operatorname{erf}\left(\frac{d}{\sqrt{2}\sigma}\right) + \frac{W + B}{2}
\end{aligned}$$

where erf is the error function

$$\operatorname{erf}(t) = \frac{2}{\sqrt{\pi}} \int_0^t e^{-x^2} dx, \quad (10)$$

implemented by most numerical program language, like C and Matlab. Using integration by parts, we can obtain the integral

$$\int_a^b \operatorname{erf}(t) dt = \frac{e^{-t^2}}{\sqrt{\pi}} + t \operatorname{erf}(t) \Big|_a^b, \quad (11)$$

and integrate again we get

$$\int_a^b \left[\frac{e^{-t^2}}{\sqrt{\pi}} + t \operatorname{erf}(t) \right] dt = \frac{1}{4} (2t^2 + 1) \operatorname{erf}(t) + \frac{e^{-t^2} t}{2\sqrt{\pi}} \Big|_a^b. \quad (12)$$

From above two equations, we then can obtain the i -th pixel value by performing integral over a rectangular region centered at (x_i, y_i) . For the sake of brevity, we have omitted parameters $\mathbf{q}, \theta, \sigma$ from main expression and leaved the de-

pendence to its variable α and δ_k

$$\begin{aligned}
& \mathcal{I}_p(i|\mathbf{q}, \theta, \sigma) \\
&= \int_{y_i - \frac{1}{2}}^{y_i + \frac{1}{2}} \int_{x_i - \frac{1}{2}}^{x_i + \frac{1}{2}} \mathcal{I}_b(\mathbf{p}|d, \sigma) dp_x dp_y \\
&= \alpha \sum_{k=1}^4 s_k \left[(2\delta_k^2 + 1) \operatorname{erf}(\delta_k) + \frac{2}{\sqrt{\pi}} e^{-\delta_k^2} \delta_k \right] + \beta
\end{aligned} \quad (13)$$

where

$$\alpha(\theta, \sigma) = \frac{(W - B)\sigma^2}{2 \sin(2\theta)}, \quad \beta = \frac{W + B}{2}, \quad (14)$$

and δ_k is the distance function Eq. 7 of four corner of pixel to the line, with a scaling factor

$$\delta_k(\theta, \mathbf{q}, x_i, y_i) = \frac{1}{\sqrt{2}\sigma} d((x_i + r_k, y_i + t_k)|\mathbf{q}, \theta). \quad (15)$$

Table 1. Coefficients in Eqs. (13)

and (15)							
k	s_k	r_k	t_k	k	s_k	r_k	t_k
1	-1	-1/2	-1/2	3	-1	+1/2	+1/2
2	+1	+1/2	-1/2	4	+1	-1/2	+1/2

The coefficient s_k, r_k , and t_k is given in Tab. 1. Similar integral form in Eq. (13) was first introduced in [1] for the purpose of constructing feature detector; however, to best of our knowledge, explicit result of this integral has never appeared in the literature aside from this paper. Compare with Eq. (9) we can find that both of them has two part, one is the average intensity, another equals intensity difference times some quantity about the distance of point to line. For pixel value, it also contains a factor with respect to θ and σ .

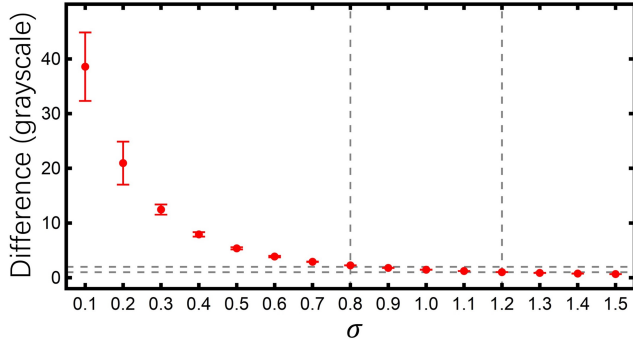


Figure 3. **Maximum intensity difference between pixel integration and pixel center.** The maximum difference between formulas Eq. (13) and Eq. (9) in a 10×10 pixel region centered at \mathbf{q} . For each σ , we repeated the experiment 500 times; the points represent the mean, and the length of the error bars represents the standard deviation. The feature center is randomly selected within a one-pixel range, and the angle is randomly chosen between $[0, \pi/4]$. $W = 200$ and $B = 50$ for typical gray scale. The two horizontal dashed lines indicate one and two gray levels, respectively. The vertical dashed lines represent the closest corresponding σ , with maximum intensity difference of 2.25 and 1.03.

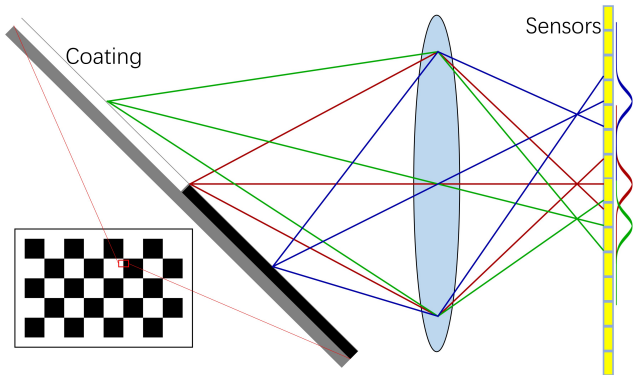


Figure 4. **Defocus in calibration.** The vertical distances between the image point, the object point, and the lens satisfy the Gaussian lens formula. The image point may not fall precisely on the sensor plane, leading to defocus. This effect can be quantitatively modeled as convolution of the point spread function (curves on the far right) and in-focus image.

Fig. 3 shows the difference between Eq. (13) and Eq. (9), where letter use the center position of pixel. We randomly select the tilt angle of the line and randomly vary the position of \mathbf{q} within the range of one pixel. It can be observed that, under typical image parameters, the maximum difference between the pixel center intensity and the pixel value becomes negligible when σ approaches one pixel. This condition is easily satisfied during calibration.

3.3. Refinement via symmetry

For the formulas provided in the previous section, a direct approach is to perform nonlinear optimization on the pixel values. Considering that the checkerboard corners are the intersection points of two lines, for the effects of aliasing in checkerboard corner’s center, though the pattern using a display device proposed by Ha et al. [11] can be used to mitigate it. However, using a display is not the optimal choice in all calibration scenarios, and the refraction correction of display screen may introduce extra errors.

Schöps et al. developed a feature refinement method that can be applied to a multi-intersecting line pattern [27], which is a generation of checkerboard. Their method was to minimize a symmetrical function

$$\arg \min_{\mathbf{H}} \sum_{i=1}^n (I(\mathbf{H}(\mathbf{s}_i)) - I(\mathbf{H}(-\mathbf{s}_i)))^2, \quad (16)$$

where \mathbf{s}_i is the position in world coordinate centered at every pattern center, and \mathbf{H} is the homography that projects the world coordinate into image pixels. By using the Levenberg-Marquardt(LM) algorithm, they estimates the homography matrix for every feature, the result points was derived from the homography matrix. This method makes amazing result. For eight intersecting line pattern, they reduce the medium reprojection errors to less 1/4 of OpenCV method with infrared camera.

However, we believe this method has two limitations: Firstly, Eq. (16) implicitly assumes that the image is captured by a pinhole camera of a continuous physical pattern, this holds for infrared camera since the surface temperature of an object can hardly change abruptly. But for visible light cameras, which captures light reflected by objects, abrupt changes can occur within the range of a single pixel[29]. In calibration, the blur in image is mainly caused by defocus, see Fig. 4. Secondly, distortion may also leads to a poor initialization of LM algorithm. Moreover, although straight lines can still be considered straight in a small neighborhood despite distortion, which is why the chessboard method is effective. But when number of intersection lines large than two, the mapping of these lines may not be described by a homography under distortion.

Now let’s do a more physical modification of Eq. (16) for visible light camera. Within the pixel ranges used for calibration, the Gaussian σ of kernel function can be considered a constant. This assumption works well even with large defocus up to several tens of pixels [12], though in that case we should consider the environment light change. We cannot use a single homography matrix to describe this mathematical relationship. A homography matrix has eight degrees of freedom and can be determined by the correspondence of four pairs of points. Considering two intersecting lines in a checkerboard pattern, a homography matrix can

be computed by selecting a bounding box around any one of the blur lines. However, the pixels near the other blur line are not necessarily determined by this matrix. In fact, the other line can be at any arbitrary angle. But from Eq. (9), we can see that as long as two points are on the same side of the half-plane and equidistant from the boundary line, they have the same value. Furthermore, when another line exists, i.e., in the standard checkerboard pattern, if two points are symmetric with respect to the feature point \mathbf{q} , then they have the same value. Therefore, we can formulate the following optimization objective

$$\arg \min_{\mathbf{q}} \sum_i [\mathcal{I}_p(\mathbf{q} + \Delta_i) - \mathcal{I}_p(\mathbf{q} - \Delta_i)]^2. \quad (17)$$

Similar to [27], we randomly sample sub-pixel points Δ_i and then optimized it by LM algorithm. The Jacobian is calculated by bilinear interpolation of the discrete gradient as well. Notice that Eq. (17) only requires the symmetry of kernel function, we actually do not need to know the analytical expression of \mathcal{I}_p .

4. Experiment

4.1. Setup

Many previous studies have achieved excellent results on synthetic data but performed a little bit poorly on real data; therefore, we directly use real data for evaluation. To date, there is no widely recognized calibration test dataset that includes the ground truth of camera parameters, so we make our own like other researchers. We primarily evaluate our results on two datasets: one captured by the infrared camera of an Intel RealSense D435 and visible light camera HIKVISION MV-SC2005AM. The latter has more noise and distortion compared to the former. The reason we chose latter is that RGB cameras may exhibit purple fringing, which could affect our assumptions. In this paper, we focus more on the impact of defocus on calibration, so we selected a camera that captures grayscale images. Besides, we want to know how distortion will affects the algorithms we compare. We evaluate accuracy using the widely used reprojection error, which projects world points into image coordinates using estimated camera parameters and then calculate the difference of extracted feature coordinates and projected positions.

We compared the performance of three methods: OpenCV, Ref. [27] and ours. Here, we are not concerned with the success rate of detection, although that is another topic worth discussing [9, 23]. We focus solely on the accuracy of sub-pixel refinement, thus using initial feature values obtained from OpenCV. Due to variations among different calibration optimization algorithms, we consistently use OpenCV’s implementation for all feature refinement methods, which initializing with Zhang’s method [33] and em-

ploying a third-order radial and second-order tangential distortion model[8] as Eqs. 1 and 2, followed by LM method up to 30 iterations.

4.2. Results

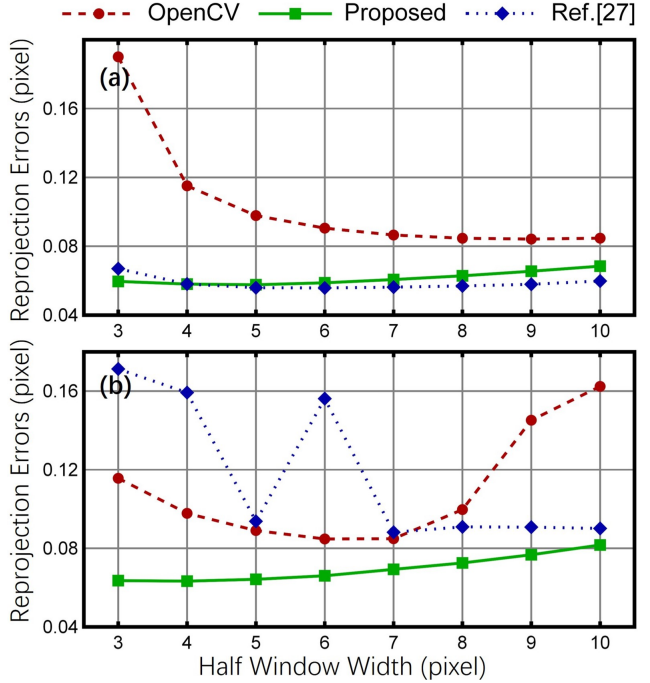


Figure 5. **Average reprojection errors with changing window size.** (a) Infrared camera of Intel Realsense D435, with resolution of 1280×800 and FOV of $90^\circ \times 64^\circ$. (b) Visible light camera of HIKVISION MV-SC2005AM, with resolution of 800×600 and FOV of $94^\circ \times 73^\circ$. All algorithms locate checkerboard corners and refine them using OpenCV first, then execute different optimization algorithms within a window. The full window width is $2 \times$ (half window width) + 1.

We have noticed that few studies discuss the impact of the optimization window on accuracy in refinement algorithms. Some, like Refs. [7] and [27], mention using a fixed window for their experimental data. However, we observe that, especially in cases with large distortion and perspective effects, the impact of the optimization window size on accuracy can exceed the differences between algorithms. In Fig. 5, we show the variation of reprojection errors with optimization window size for different algorithms. Fig. 5(a) presents the results for an infrared camera, as shown in Tab. 2, the distortion of this camera is relatively small. Therefore, all algorithms achieve the best reprojection error over a large window size range. In the 3 – 10 range tested in our experiments, methods of this paper and Ref. [27] significantly outperform OpenCV’s method. The reprojection error for OpenCV stabilizes as the window size increases, while both methods of this paper and Ref. [27] show a

slight decrease from 3 to 4, followed by a slow rise, with Ref. [27]’s method rising more slowly. As seen in Tab. 2, for the optimal reprojection error, our method is similar to Ref. [27]. Compared to OpenCV, our method reduces the mean and median reprojection errors by 33.7% and 33.9%, respectively.

Fig. 5(b) shows the results for visible light camera. Compared to the infrared camera we used, it has a lower resolution and a wider field of view. As seen in Tab. 2, it has larger camera distortion. In this case, the accuracy of both the OpenCV and Ref. [27]’s methods fluctuates significantly with the change in window size. In particular, Ref. [27]’s method shows an overall decrease, but with a fluctuation around size 6. We believe this is mainly due to the inappropriate physical assumptions of this method in this situation, as discussed earlier. Additionally, we observed some sample points fell outside the image boundaries during the algorithm’s execution, which is caused by difficulties in initializing the homography matrix due to distortion and noise, while the LM algorithm is sensitive to initial values. We discarded these points. However, the same algorithm did not encounter this issue in any of the windows for the infrared camera. For OpenCV, its overall error decreases first and then increases, achieving good reprojection error only in the narrow window size range of 5–7. When the window size increases to 10, Ref. [27]’s method reduces the error by almost 50% compared to OpenCV. For the optimal error, we significantly outperform both methods, reducing the mean and median reprojection errors by 26.9% and 18.5% compared to Ref, and by 25.0% and 25.0% compared to OpenCV.

Tab. 2 presents the estimated parameters, distortion coefficients are from Eqs. 1 and 2. For the infrared camera, our results are similar to those of the Ref. [27]. For the visible light camera, the camera matrix parameters estimated by the Ref. [27] are similar to ours, while the distortion parameters align more closely with those of OpenCV. Fig. 6 shows the distribution of the reprojection error. In the visible light camera case, the reference method produces large errors in several views. In the blue-colored view, 2–3 outliers are observed in our method, which corresponds to the viewpoint with the highest reprojection error using the OpenCV method. The primary cause is that, in this view, some feature points are significantly farther from the camera’s z-axis, leading to higher noise levels. While this issue can be solved through such as manual correction by MATLAB toolbox, we decided to keep the original outcomes of algorithm.

5. Discussions

Conclusion In this paper, we proposed a novel feature extraction method for camera calibration, addressing the limitations of existing approaches, particularly for visible light

camera cameras under defocus and distortion conditions. Our objective function, which accounts for blur nature of optical defocus, simplifies computation and reduces the risk of overfitting for symmetry based method proposed by Schöps et al.. Through experiments on real-world data from both infrared and visible light camera cameras, we demonstrated that our method significantly improves reprojection error compared to OpenCV and approach by Schöps et al.. Specifically, we achieved a mean and medium reprojection error reduction of 26.9% and 18.5% than Schöps et al. for visible light camera cameras with large distortion. For infrared case, we get a similar result with optimal refinement window size. In both types of cameras, we achieved significantly better results compared to OpenCV, reduce reprojection error 25.0% to 33.9%. We also discussed the impact of optimization window size on the algorithms and found that it is important for cameras with large distortion. In such cases, OpenCV is highly sensitive to the optimization window size, while our method is more robust.

We discussed two different causes of blurred images and explained why the method by Schöps et al. is not suitable for visible light cameras. For visible light cameras, we considered the Gaussian point spread function blur model for straight edges of checkerboard patterns and provided an analytical solution for discrete pixel values. This is significant for further calibration methods based on deconvolution, as well as precise localization in applications like QR code detection. Our calculations show that when defocus is small, there is a significant difference between point intensity and pixel intensity, which may lead to more accurate results in current single-image depth from defocus methods based on point intensity.

In conclusion, our method offers a significant improvement in feature extraction accuracy for camera calibration, especially in real-world scenarios where distortion, defocus, and challenging poses are present. These findings suggest that our approach is well-suited for practical applications in 3D vision, autonomous systems, and multi-sensor environments, where reliable and accurate calibration is critical.

Limitations and feature works For the visible light camera, we calibrated not only industrial cameras but also smartphone cameras. Although our method still achieved better results than OpenCV, the difference was not as significant as we expected. We observed noticeable purple fringing in the smartphone camera when capturing the checkerboard pattern, which may be caused by chromatic aberration. Therefore, there is room for algorithmic improvement for cheap digital cameras. Another issue is, although our experiments show that the method by Schöps et al. is not optimal for visible light cameras, it still achieved significantly better results than OpenCV with the star pattern they proposed. This is because, as explained by Datta et al., the assumptions of the OpenCV method only hold for non

Methods	Reprojection error		Camera matrix				Distortion($\times 10^{-3}$)				
	Average	Medium	f_x	f_y	c_x	c_y	k_1	k_2	k_3	p_1	p_2
Infrared camera											
OpenCV	0.0842	0.0635	640.55	642.15	643.42	400.23	4.82	-10.00	5.85	0.07	0.35
Proposed	0.0576	0.0430	640.75	642.34	643.54	400.31	4.30	-7.55	4.15	0.14	0.42
Ref. [27]	0.0561	0.0420	640.80	642.41	643.52	400.33	4.34	-7.60	4.19	0.16	0.40
Visible light camera											
OpenCV	0.0848	0.0627	471.07	470.93	386.14	296.41	27.53	-74.05	16.00	-0.19	-0.12
Proposed	0.0636	0.0470	471.30	471.17	386.24	296.43	24.88	-68.17	11.76	-0.19	-0.09
Ref. [27]	0.0870	0.0577	471.29	471.16	386.04	296.47	27.71	-76.89	16.34	-0.17	-0.29

Table 2. **Reprojection errors and camera parameters.** The camera description can be seen in caption of Fig. 5, with all results corresponding to the optimal window for each method. For the infrared camera, our results are similar to those of the Ref. [27], which is slightly better than ours and significantly better than OpenCV. For the visible light camera, we achieved the best results. The median error of the Ref. [27] is better than that of OpenCV, while the average error is slightly worse. Their camera matrix parameters are similar to ours, while the distortion parameters are similar to those of OpenCV.

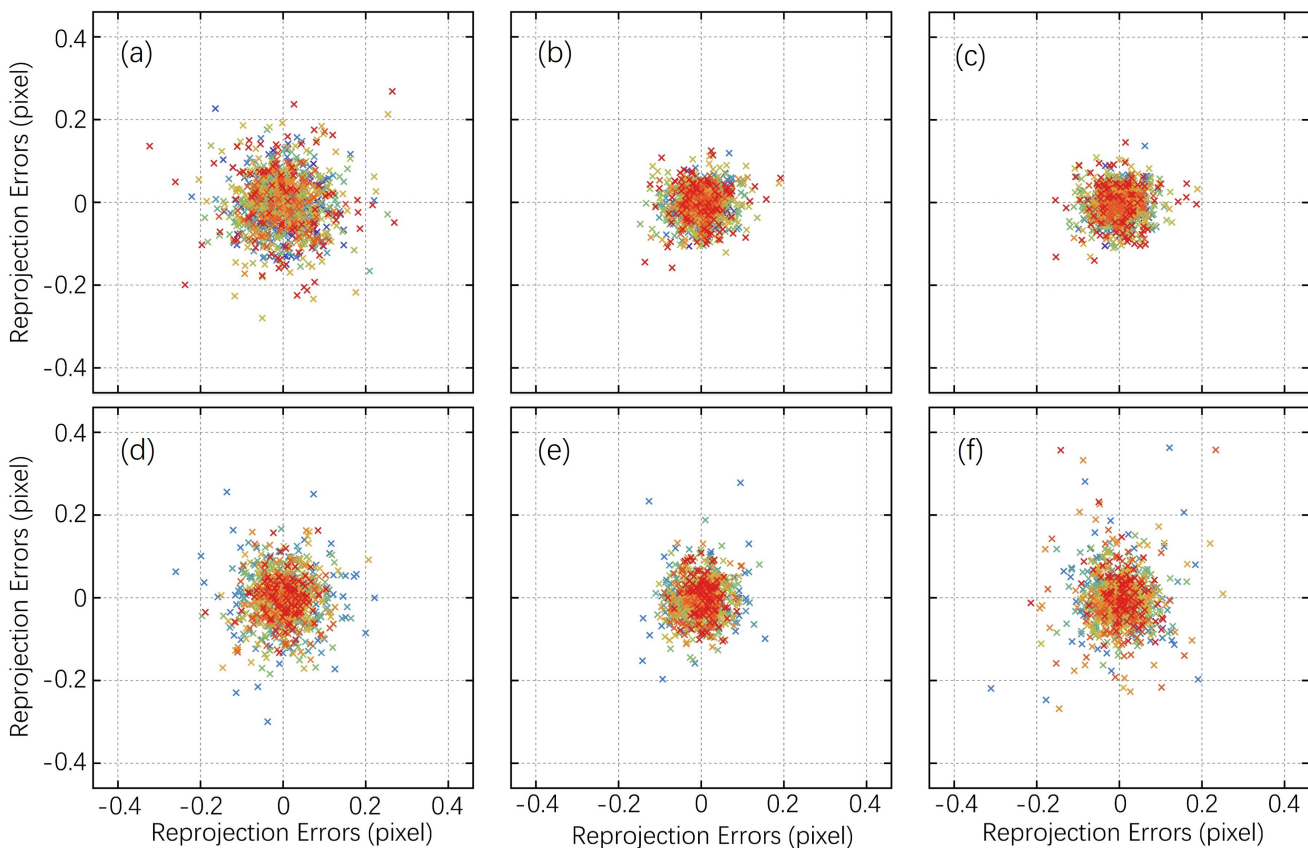


Figure 6. **Vector representation of reprojection errors.** The difference between the reprojection points and the image points, with different colors representing different camera views. The images above, labeled (a)-(c), correspond to the infrared camera, while the images below, labeled (d)-(f), correspond to the visible light camera. The left column represents the OpenCV method, the middle column represents our method, and the right column represents method of Ref. [27].

fronto-parallel input images, meaning at most two intersecting lines meet the assumptions, which limits its ability to effectively utilize the information from all lines. However, as reported by Schöps et al. increasing the number of inter-

section lines on the star pattern beyond 16 does not further enhance accuracy. How to resolve aliasing at the center of star based pattern to achieve higher precision remains to be studied further. This will be a direction for our future work.

References

- [1] Simon Baker, Shree K Nayar, and Hiroshi Murase. Parametric feature detection. *International Journal of Computer Vision*, 27(1):27–50, 1998. 2, 3, 4
- [2] Jean-Yves Bouguet. Camera calibration toolbox for matlab. 2022.
- [3] Bolin Cai, Yuwei Wang, Jiajun Wu, Mengyu Wang, Fei Li, Mengchao Ma, Xiangcheng Chen, and Keyi Wang. An effective method for camera calibration in defocus scene with circular gratings. *Optics and Lasers in Engineering*, 114:44–49, 2019. 3
- [4] Ankur Datta, Jun-Sik Kim, and Takeo Kanade. Accurate camera calibration using iterative refinement of control points. In *2009 IEEE 12th International Conference on Computer Vision Workshops, ICCV Workshops*, pages 1201–1208. IEEE, 2009. 2
- [5] Frederic Devernay and Olivier Faugeras. Straight lines have to be straight. *Machine vision and applications*, 13:14–24, 2001. 1
- [6] C Brown Duane. Close-range camera calibration. *Photogramm. Eng.*, 37(8):855–866, 1971. 1
- [7] Alexander Duda and Udo Frese. Accurate detection and localization of checkerboard corners for calibration. In *BMVC*, 2018. 2, 6
- [8] John G Fryer and Duane C Brown. Lens distortion for close-range photogrammetry. *Photogrammetric engineering and remote sensing*, 52:51–58, 1986. 1, 3, 6
- [9] Peter Fuersattel, Sergiu Dotenco, Simon Placht, Michael Balda, Andreas Maier, and Christian Riess. Occlud—occluded checkerboard pattern detector. In *2016 IEEE Winter Conference on Applications of Computer Vision (WACV)*, pages 1–9. IEEE, 2016. 6
- [10] Wolfgang Förstner and Eberhard Gülch. A fast operator for detection and precise location of distinct points, corners and centres of circular features. In *Proc. ISPRS intercommission conference on fast processing of photogrammetric data*, pages 281–305. Interlaken, 1987. 2
- [11] Hyowon Ha, Yunsu Bok, Kyungdon Joo, Jiyoung Jung, and In So Kweon. Accurate camera calibration robust to defocus using a smartphone. In *Proceedings of the IEEE International conference on computer vision*, pages 828–836, 2015. 2, 3, 5
- [12] Hyowon Ha, Michal Perdoch, Hatem Alismail, In So Kweon, and Yaser Sheikh. Deltile grids for geometric camera calibration. In *Proceedings of the IEEE International Conference on Computer Vision*, pages 5344–5352, 2017. 2, 5
- [13] Richard Hartley and Andrew Zisserman. *Multiple view geometry in computer vision*. Cambridge university press, 2003. 3
- [14] Janne Heikkilä. Geometric camera calibration using circular control points. *IEEE Transactions on pattern analysis and machine intelligence*, 22(10):1066–1077, 2000. 2
- [15] Janne Heikkilä and Olli Silven. Calibration procedure for short focal length off-the-shelf ccd cameras. In *Proceedings of 13th International Conference on Pattern Recognition*, pages 166–170. IEEE, 1996. 2
- [16] Daniel Herrera, Juho Kannala, and Janne Heikkilä. Joint depth and color camera calibration with distortion correction. *IEEE Transactions on Pattern Analysis and Machine Intelligence*, 34(10):2058–2064, 2012. 1
- [17] Junzhou Huo, Haidong Zhang, Zhichao Meng, Fan Yang, and Guiyu Yang. A flexible calibration method based on small planar target for defocused cameras. *Optics and Lasers in Engineering*, 157, 2022. 2
- [18] Juho Kannala and Sami S Brandt. A generic camera model and calibration method for conventional, wide-angle, and fish-eye lenses. *IEEE transactions on pattern analysis and machine intelligence*, 28(8):1335–1340, 2006. 1
- [19] Kang Liao, Lang Nie, Shujuan Huang, Chunyu Lin, Jing Zhang, Yao Zhao, Moncef Gabbouj, and Dacheng Tao. Deep learning for camera calibration and beyond: A survey. *arXiv preprint arXiv:2303.10559*, 2023. 1
- [20] Luca Lucchese and Sanjit K Mitra. Using saddle points for subpixel feature detection in camera calibration targets. In *Asia-Pacific Conference on Circuits and Systems*, pages 191–195. IEEE, 2002. 2
- [21] Zhichao Meng, Haidong Zhang, Doudou Guo, Shangqi Chen, and Junzhou Huo. Defocused calibration for large field-of-view binocular cameras. *Automation in Construction*, 147:104737, 2023. 2, 3
- [22] Vishvjit S Nalwa and Thomas O Binford. On detecting edges. *IEEE transactions on pattern analysis and machine intelligence*, (6):699–714, 1986. 3
- [23] Simon Placht, Peter Fürsattel, Etienne Assoumou Mengue, Hannes Hofmann, Christian Schaller, Michael Balda, and Elli Angelopoulou. Rochade: Robust checkerboard advanced detection for camera calibration. In *Computer Vision—ECCV 2014: 13th European Conference, Zurich, Switzerland, September 6–12, 2014, Proceedings, Part IV 13*, pages 766–779. Springer, 2014. 6
- [24] Zoltan Pusztai and Levente Hajder. Accurate calibration of lidar-camera systems using ordinary boxes. In *Proceedings of the IEEE international conference on computer vision workshops*, pages 394–402, 2017. 1
- [25] Srikumar Ramalingam and Peter Sturm. A unifying model for camera calibration. *IEEE transactions on pattern analysis and machine intelligence*, 39(7):1309–1319, 2016. 1
- [26] Thomas Schöps, Torsten Sattler, and Marc Pollefeys. Bad slam: Bundle adjusted direct rgb-d slam. In *Proceedings of the IEEE/CVF Conference on Computer Vision and Pattern Recognition*, pages 134–144, 2019. 2
- [27] Thomas Schöps, Viktor Larsson, Marc Pollefeys, and Torsten Sattler. Why having 10,000 parameters in your camera model is better than twelve. In *Proceedings of the IEEE/CVF Conference on Computer Vision and Pattern Recognition*, pages 2535–2544, 2020. 2, 5, 6, 7, 8
- [28] Chaehyeon Song, Jaeho Shin, Myung-Hwan Jeon, Jongwoo Lim, and Ayoung Kim. Unbiased estimator for distorted conics in camera calibration. In *Proceedings of the IEEE/CVF Conference on Computer Vision and Pattern Recognition*, pages 373–381, 2024. 2
- [29] Agustín Trujillo-Pino, Karl Krissian, Miguel Alemán-Flores, and Daniel Santana-Cedrés. Accurate subpixel edge location

- based on partial area effect. *Image and vision computing*, 31(1):72–90, 2013. 2, 3, 5
- [30] Rafael Grompone von Gioi and Gregory Randall. A sub-pixel edge detector: an implementation of the canny/devernay algorithm. *Image Processing On Line*, 7:347–372, 2017. 3
- [31] Shaoan Wang, Mingzhu Zhu, Yaoqing Hu, Dongyue Li, Fulong Yuan, and Junzhi Yu. Accurate detection and localization of curved checkerboard-like marker based on quadratic form. *IEEE Transactions on Instrumentation and Measurement*, 71:1–11, 2022. 2
- [32] Yuwei Wang, Lu Liu, Bolin Cai, Keyi Wang, Xiangcheng Chen, Yajun Wang, and Bo Tao. Stereo calibration with absolute phase target. *Optics Express*, 27(16):22254–22267, 2019. 3
- [33] Zhengyou Zhang. A flexible new technique for camera calibration. *IEEE Transactions on pattern analysis and machine intelligence*, 22(11):1330–1334, 2000. 1, 6
- [34] Hongbo Zhao, Yikang Zhang, Qijun Chen, and Rui Fan. Dive deeper into rectifying homography for stereo camera online self-calibration. In *2024 IEEE International Conference on Robotics and Automation (ICRA)*, pages 14479–14485. IEEE, 2024. 1
- [35] Shaojie Zhuo and Terence Sim. Defocus map estimation from a single image. *Pattern Recognition*, 44(9):1852–1858, 2011. 3